Catchment landforms predict groundwater-dependent wetland sensitivity to recharge changes

Etienne Marti¹, Sarah Leray^{1,2}, Clément Roques³

- ¹ Departamento de Ingeniería Hidráulica y Ambiental, Pontificia Universidad Católica de Chile, Santiago, Chile
- ²Centro de Cambio Global UC, Santiago, Chile
- ³ Centre for Hydrogeology and Geothermics (CHYN), University of Neuchâtel, Neuchâtel, Switzerland

Correspondence to: Clément Roques (clement.roques@unine.ch)

Abstract. This study investigates the influence of topography on the desaturation rates of groundwater-dependent wetlands in response to changes in recharge. We examined 60 catchments across northern Chile, which feature a wide variety of landforms. Landforms were categorized using geomorphon descriptors, resulting in three distinct clusters: flat, transitional, and mountain settings. Using steady-state 3D groundwater models, we derived flow partitioning and seepage area extent for each catchment. Each cluster exhibited consistent seepage areas evolution under varying wet-to-dry conditions. Our findings indicate that mountains have reduced seepage area compared to flats at equivalent hydraulic conductivity to recharge (K/R) ratios, but are less sensitive to recharge fluctuations, with slower rates of seepage area reduction. Statistical analyses show that geomorphon-defined landforms correlate with desaturation indicators, enabling the prediction of catchment sensitivity to climate change based solely on a topographic attributes.

Short summary. This study shows that the response of groundwater-dependent wetlands to recharge changes can be predicted from landform properties alone. Mountain catchments are less sensitive to recharge changes than flat ones, due to fewer but more persistent seepage areas. These results support a scalable approach to assessing wetland vulnerability to climate change, with practical implications for water resource management and conservation planning in diverse landscapes.

1. Introduction

Changes in precipitation regimes and increasing temperatures driven by climate change are anticipated to significantly affect both surface and subsurface water resources (Berghuijs et al., 2024; Konapala et al., 2020; Taylor et al., 2013). Extended drought periods and reduced recharge are expected to threaten the functioning of groundwater-dependent ecosystems (Kløve et al., 2014; Rohde et al., 2024; Tetzlaff et al., 2024). These ecosystems rely on groundwater contributions to maintain their ecological structure and functional integrity, including processes that support biodiversity and key ecosystem services (Barron et al., 2014; Doody et al., 2017; Eamus & Froend, 2006). They encompass both terrestrial and aquatic environments, including wetlands, springs, rivers (riparian, aquatic, and hyporheic zones), lakes, grasslands, forests, as well as coastal and estuarine habitats (Eamus & Froend, 2006; Kløve et al., 2011). The extent to which groundwater-dependent ecosystems are vulnerable

to climate-induced reductions in recharge depends not only on the hydrogeological properties of the underlying aquifer, but also on the role of landscape morphology in shaping groundwater flow and discharge patterns (Gleeson & Manning, 2008; Singha & Navarre-Sitchler, 2022). Identifying the physical controls on groundwater emergence at the land surface is therefore essential to improve our ability to anticipate groundwater-dependent ecosystems responses to climate variability.

Groundwater seepage occurs when the water table intersects the topography. Thus, landforms influence both its spatial distribution and temporal dynamics (Bresciani et al., 2014, 2016; Sophocleous, 2002). The interaction between groundwater and topography significantly impacts the resilience of groundwater-dependent wetlands to climate variability (Cuthbert et al., 2019; Scanlon et al., 2023). Considering steady-state groundwater flow systems, the depth of the water table, and the distribution of flow paths and groundwater seepage areas, are controlled by the groundwater recharge rate (*R*), the topography and by the hydrodynamic properties of the aquifer through its hydraulic conductivity (*K*), (Condon & Maxwell, 2015; Rath et al., 2023; Tóth, 1963; Zhang et al., 2022). An equivalence of effects between *R* and *K* has been demonstrated (Bresciani et al., 2014; Haitjema & Mitchell-Bruker, 2005; Jamieson & Freeze, 1982), allowing a convenient focus on the dimensionless $\frac{K}{R}$ ratio and the topography. In non-anthropized contexts, the groundwater table is typically near the surface in low-relief and/or humid regions, and deeper in rugged terrain and/or arid regions. However, the hydrogeological response and seepage dynamics to varying landscapes and topographic features are not straightforward and difficult to predict.

Analytical solutions have been proposed to quantify the extent of groundwater seepage under varying $\frac{K}{R}$ at the hillslope scale, using simplified groundwater flow equations (Bresciani et al., 2014, 2016). Marçais et al. (2017) conducted modeling experiments to estimate seepage extent and dynamics using a 2D representation of the equivalent hillslope. While these approaches are applicable in shallow aquifers, where flow predominantly follows the topography, they do not capture the complexity of 3D groundwater flow, especially under low water tables or steep reliefs. A few 3D numerical modeling experiments have been undertaken, mainly for sensitivity studies with conceptual surface and subsurface geometries (Carlier et al., 2019; Gauvain et al., 2021; Gleeson & Manning, 2008; Welch et al., 2012). There is a pressing need to better understand the distribution and dynamics of groundwater seepage, particularly in light of the complex topographic characteristics of real-world landscapes and the 3D nature of groundwater flow. Such knowledge is critical for predicting the extent of seepage and the persistence of groundwater-dependent wetlands under future climate scenarios.

50

To address this knowledge gap, we designed a numerical experiment to model the partitioning of 3D groundwater flow and the extent of seepage across different landscapes, from flat to high mountain settings, under varying $\frac{K}{R}$ values. We applied this experiment on 60 catchments located in northern Chile, selected for their rich diversity of geomorphological contexts. By linking key topographic characteristics of the catchments to groundwater seepage dynamics predicted by the model, we aim to improve the prediction of wetland desaturation sensitivity under changing climate conditions. This approach supports the development of transferable frameworks for assessing the vulnerability of groundwater-dependent ecosystems across heterogeneous terrain and provide statistical means to regionalize our findings.

2. Material and Methods

2.1. Geomorphological context

65 The study area is located in northern Chile between Santiago and the Peruvian border. The landforms diversity results from the specific tectonic and weathering processes involved in the Andes. This process resulted in the formation of a longitudinal valley called the Central Depression, which is bounded by two cordilleras, the Coastal Cordillera and the Principal Cordillera, both composed mainly of volcanic-sedimentary rocks (Hartley & Evenstar, 2010; Jordan et al., 1983). The Coastal Cordillera forms an intermediate mountain range with an average elevation between 1,000 and 2,000 m.a.s.l., while the Principal Andean Cordillera has maximum elevations close to 7,000 m.a.s.l. (Figure 1a) (Armijo et al., 2015; Charrier et al., 2007). The Central Depression delineates a sedimentary basin rich in Quaternary alluvial deposits with variable thicknesses, ranging from about 250 m near Santiago (Yáñez et al., 2015) to almost 1,000 m in the northern regions of Chile (Hartley & Evenstar, 2010; Jordan et al., 2014; Nester & Jordan, 2011). Specifically, the Pre-Cordillera is a transition zone between the Central Depression and the Western Cordillera, with catchment characteristics that vary from nearly flat terrain to mountainous regions with steep slope gradients and typical mountain front geomorphology (Figure 1a). The diversity of these environments provides an excellent opportunity to explore a wide range of topographic settings, including flat catchments, mountain-front areas, incised mountain catchments, volcanoes, and high mountain peaks.

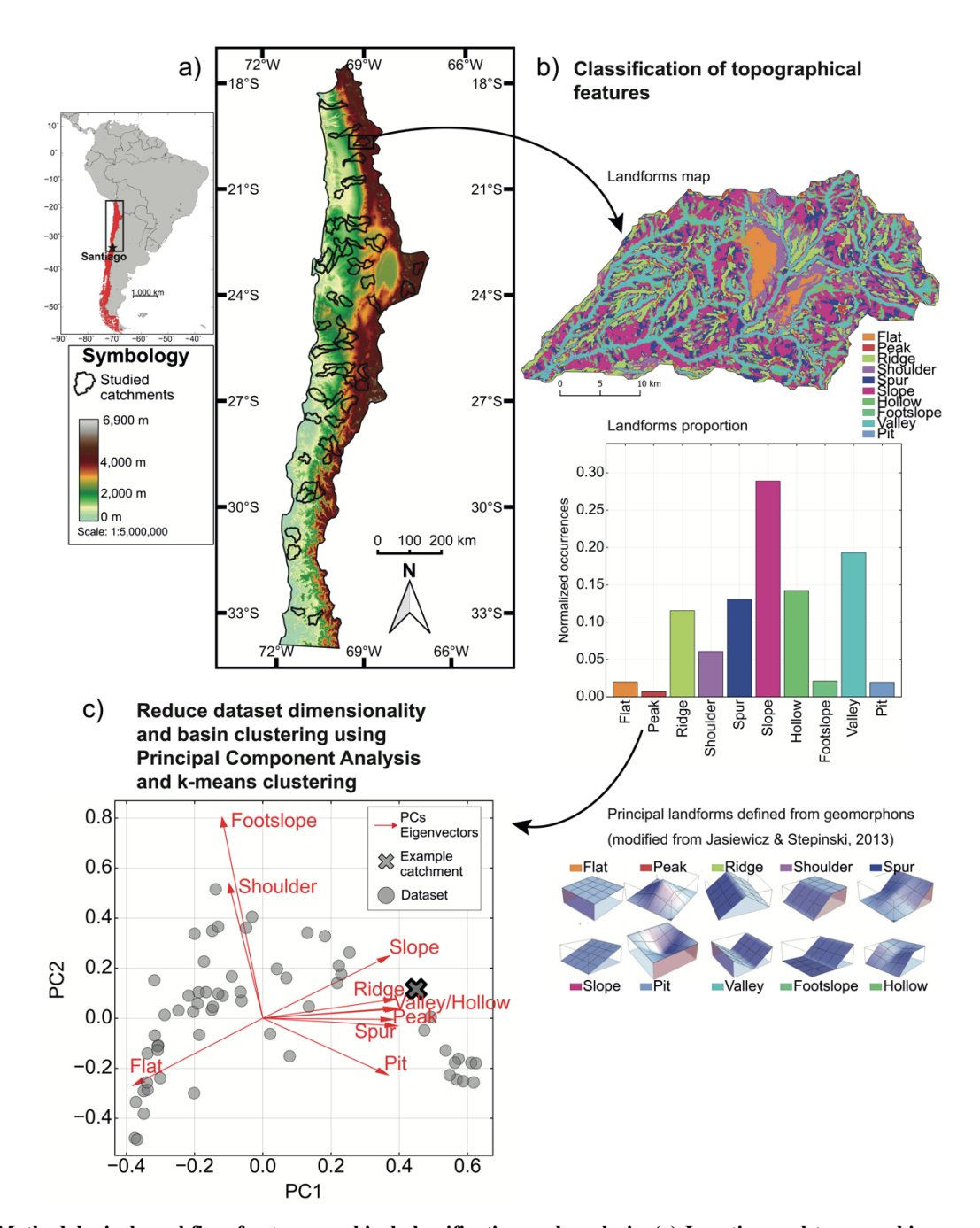


Figure 1: Methodological workflow for topographical classification and analysis. (a) Location and topographic map of the study area in northern Chile, with the boundaries of the 60 studied catchments highlighted in black. (b) Example of landform classification within a single catchment, including a landform map, the proportion of landform types, and an illustration of the principal landform categories defined by geomorphons (adapted from Jasiewicz & Stepinski, 2013). (c) Catchment categorization using Principal Component Analysis (PCA) for dimensionality reduction and clustering. The example catchment is plotted in the PCA space, illustrating its position relative to the first two principal components (PC1 and PC2) and the whole dataset (grey dots). Red arrows represent the eigenvectors associated with different landform types, showing their contribution to the PCA axes.

2.2. Classification of catchment topographies

We considered the catchment boundaries of the global catchment database HydroATLAS (Lehner & Grill, 2013). We chose to limit the size of the catchments to between 500 and 1,500 km² by considering level 8 of HydroATLAS. To cover different geomorphological and tectonic settings, we selected 60 catchments within our study area (indicated by black boundaries in Figure 1a). We extracted the topography from the SRTM (Shuttle Radar Topography Mission, 90 m resolution) digital elevation model (DEM).

We used the geomorphons classification method proposed by Jasiewicz & Stepinski (2013) to categorize the landform features within each catchment; e.g., *flat, peak, ridge, shoulder, spur, slope, pit, valley, footslope, and hollow.* (Figure 1b, note that geomorphons-defined landforms are italicized throughout the text for improved readability). This methodology is based on elevation differences in eight directions relative to the reference cell. This operation is reproduced for each cell of the DEM, identifying a shape for each of these cells (Figure 1b). Unlike the direct cell neighbor method (e.g., slope, curvature, or roughness), the geomorphons method allows for capturing landforms at larger scales by defining a search radius around the reference cell, the look-up distance in Jasiewicz & Stepinski (2013). Here we defined the search radius equal to the hillslope characteristic length:

$$L = \frac{1}{2D} \to L = \frac{1}{2*\frac{l}{4}},$$
 (1)

where *L* is the catchment feature length, *l* is the river network length, *D* is the drainage density, and *A* is the catchment area. The river network is defined using a surface flow accumulation routine available in the Whitebox tool Python package (Lindsay, 2016). Combining principal component analysis (PCA) and k-means clustering methods (Figure 1c), we categorized the catchments by their dominant landform features (Figure 1b). PCA is a classical statistical method used to reduce the dataset dimensionality by transforming the original variables into a new set of uncorrelated variables, called principal components (PC), which capture the maximum variance in the data. The k-means clustering approach allows us to identify groups of catchments belonging to the cluster with the nearest mean within the new PC space (Figure 1c). Here, we defined 3 main clusters of catchments typical of flat, transitional, and mountain settings. Python code and trained models are available on the repository(Marti et al., 2025).

2.3. Numerical modeling of groundwater seepage extent

115

A three-dimensional numerical groundwater flow model was developed for each catchment. The models were constructed and run using the MODFLOW-2005 software suite (Harbaugh, 2005) with the NWT solver (Niswonger et al., 2011), and managed through the Python-based interface FLOPY (Bakker et al., 2016). The diffusivity equation was solved under steady-state conditions for unconfined flow.

The horizontal discretization followed the DEM resolution, set at 90 meters (Figure 2a), while the vertical discretization consisted of ten layers with exponentially increasing thickness (Figure 2b). To limit boundary effects, a buffer zone extending

the model domain by 20% around each catchment was added. A sensitivity analysis (Abhervé et al., 2023) of the extent of the buffer zone was performed to ensure that no impact on the seepage distribution was identified within the studied catchment (Figure 2a). The model bottom mirrored the topography with a 100m-thick aquifer (Figure 2b). Assuming a constant aquifer thickness minimized the potential effects of transmissivity changes on seepage distribution. The 100m thickness was chosen to realistically accommodate both flat sedimentary catchments and steep mountainous aquifers (Condon et al., 2020). The side and bottom boundaries of the buffer box were set as no-flow. For generality, effective recharge *R* was uniformly set at the water table across both the catchment and its buffer, enabling the simulation of both inflow and outflow across the model boundaries. This setup allowed considering interbasin groundwater exchanges, which are particularly likely to occur under low water table conditions (Fan, 2019). A drain boundary condition (with a conductance equal to the product of hydraulic conductivity with horizontal cell area divided by the cell mid-thickness) was set on the topography using the eponymous packages in MODFLOW to allow exfiltration of groundwater wherever the water table rises to intersect the land surface. This method ensures that discharge occurs naturally along the topography, mimicking surface-connected wetlands and springs without imposing fixed fluxes or predefined discharge zones.

To solely focus on the effects of topography in the redistribution of groundwater seepage, we imposed homogeneous and isotropic hydraulic conductivity (K) across all modelled catchments. This simplification ensures that variability in seepage behavior arises solely from differences in landscape geometry and water table positions, rather than site-specific geological heterogeneity. Various water table positions relative to the topography were derived by setting different values of the $\frac{K}{R}$ ratio, ranging from 100 for fully saturated conditions to 10,000 when all simulated catchments reached near full desaturation (i.e., when the normalized seepage area $S_A^* = \frac{seepage\ area}{catchment\ area}$ reaches 1%). $\frac{K}{R}$ values were logarithmically spaced within this interval, and simulations were stopped if the catchment's seepage area fell below the 1% threshold (Figure 2c). This allows us to consider a full range of conditions from humid to arid climates and low- to high-hydraulic conductivity settings. This modeling workflow resulted in a total of 1,793 simulations.

For each catchment, we perform a power law fit on the relationship between seepage area extent and $\frac{K}{R}$ further mentioned as the desaturation function ((2a, and red curve in Figure 2c). This allows us to capitalize on the observed linear relation between $\log (S_A^*)$ and $\log (\frac{K}{R})$:

$$S_A^* = \left(1 + \left(\frac{K}{\overline{R}}\right)^2\right)^n \tag{2a}$$

$$\frac{dS_A^*}{d\frac{K}{R}} = \frac{2n}{\lambda^2} \frac{K}{R} \frac{S_A^*}{1 + \left(\frac{K}{R}\right)^2}$$
(2b)

$$\frac{dS_A^*}{d\frac{K}{R}} \approx \frac{2nS_A^*}{\frac{K}{R}} \text{ when } \frac{K}{R} \gg \lambda$$
 (2c)

The desaturation function is determined by the proportionality constant, λ , which can be associated with a desaturation threshold, i.e., the critical value of $\frac{K}{R}$ above which the catchment begins to desaturate. The negative desaturation exponent, n, directly affects the rate of change in seepage extent as $\frac{K}{R}$ increases, as shown in Equations 2b and 2c. It can be viewed as a measure of the sensitivity of the seepage area extent to a deepening of the water table: for a given pair of seepage area and $\frac{K}{R}$, a lower n indicates a higher sensitivity of the catchment to a decrease of the water level. We estimated n considering seepage area extents lower than 20% of the catchment area, which are more representative of real-world conditions, i.e., by giving more weight in the fit to the higher $\frac{K}{R}$ ratios.

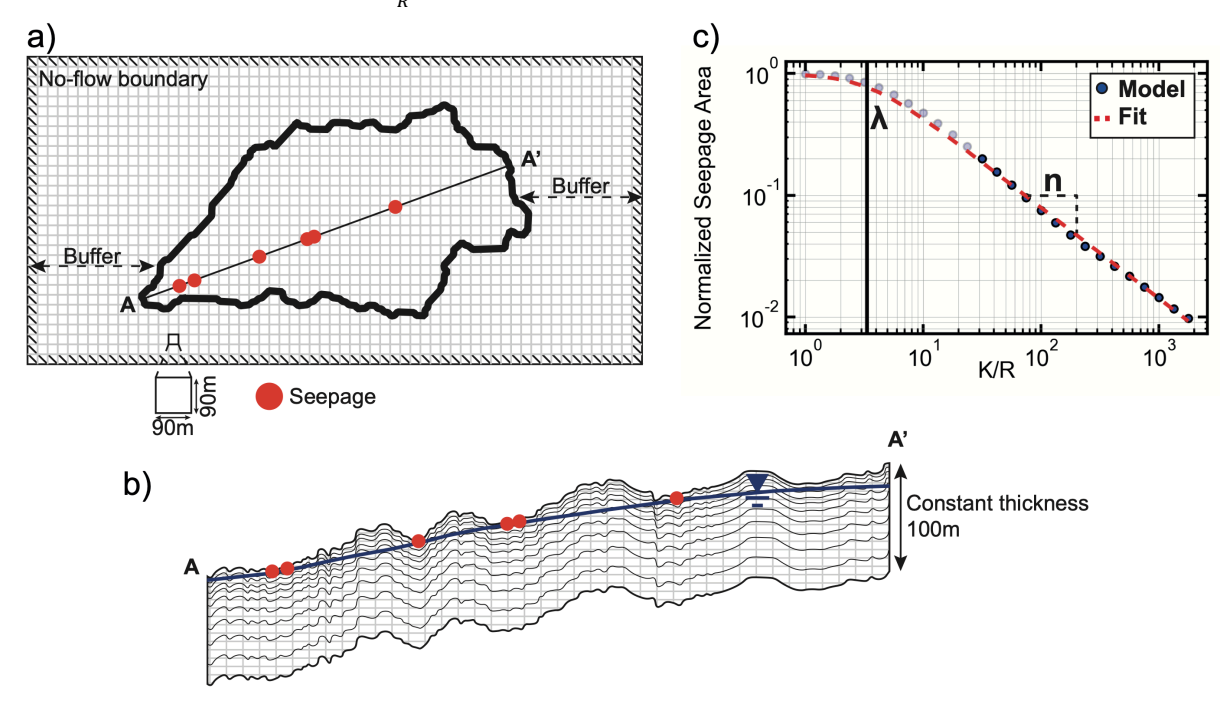


Figure 2: Model settings for one example catchment: (a) Horizontal discretization and buffer zone beyond catchment limits, (b) AA' cross-section including vertical discretization and an arbitrary water table intercepting the topography creating seepage areas (red dots), (c) Example of results of normalized seepage area with respect to K/R (grey and blue dots) with the power law fit for Eq. 2a (dashed red curve). The blue dots represent the normalized seepage area < 20% where the fit weight is enhanced.

2.4. Regionalization with Random Forest algorithm

To predict the desaturation response metrics λ and n from topographic descriptors and regionalize our findings, we employed Random Forest regression using the scikit-learn library in Python (Pedregosa et al., 2011). The input features for the model were the first two principal components (PC1 and PC2) derived from the 60 catchments. Random Forest models were trained independently for λ and n. Model performance and robustness were assessed using a bootstrap resampling procedure with 5,000 iterations. In each iteration, 10 catchments were randomly selected as a test set, while the remaining 50 were used for training. The coefficient of determination (R²) was calculated on the test data for each iteration, and the resulting R² distribution was used to evaluate model reliability (see Supplementary Material S2 for Kernel Density Estimate of R² values). Hyperparameter tuning for each model was performed using GridSearchCV with 2-fold cross-validation within each training subset. The tested parameter grid included n_estimators \in {50, 200, 500, 1000} and max_depth \in {None, 2, 10, 20}. The best combination of hyperparameters was used to retrain the model on the full training set in each iteration. The final Random Forest model was defined as the one achieving the best trade-off in predictive accuracy for both λ and n, and it was applied to predict desaturation metrics in 63 additional catchments located in South Chile.

3. Results

155

160

165

170

175

3.1. Typology of catchments topography

We evaluate the proportion of main geomorphons on the 60-catchment dataset. The PCA analysis (Figure 1c) resulted in a first component (PC1) explaining 75.4% of the total variance, and the first two components (PC1 and PC2) combined explaining 86.8% of the total variance. This result indicates a strong relation between the landforms description from geomorphons analysis in the catchments and the reduction into 2 dimensions. We found that PC1 mostly represents the differentiation between *flat* and *slope* landforms, with eigenvector magnitudes of -0.4 for the *flat* landform and 0.4 for the *slope* landform. *Slope* landform is associated with the *peak*, *ridge*, *valley*, *hollow*, *spur*, and *pit* forms, all showing similar eigenvectors magnitude on PC1. Regarding PC2, the *footslope* and *shoulder* forms are the main control with an eigenvector magnitude of respectively, 0.8 and 0.5. *Flat* and *slope* forms show eigenvectors magnitudes of -0.2 and 0.2 along the PC2 axis. To further support and illustrate this description, the catchments are grouped into three clusters, as a result of the k-means clustering, displayed with different colors in the subsequent Figures 3 and 4. The red cluster is characterized by relatively *flat* landforms. Conversely, the blue cluster is strongly influenced by *slope* and associated landforms along PC1 (*ridge*, *valley*,

peak) representative of *mountain* catchments with incised valleys and narrow valley bottoms. The green cluster exhibits more dispersion in the represented catchments. This cluster acts as a transition between the red and blue clusters. It contains catchments most influenced by *footslope* and *shoulder* forms. Positioned centrally between the two extreme clusters, this cluster serves as a transition zone between flatter areas and mountain catchments, possibly including catchments showing both flat and mountainous characteristics, as observed at mountain fronts.

To facilitate comprehension and illustration, the catchment clusters are referred to as *flat* catchment for the red cluster, *mountain* catchment for the blue cluster, and *transitional* catchment for the green cluster thereafter.

3.2. Seepage distribution evolution with increasing $\frac{K}{R}$

180

185

190

195

200

Figure 3a illustrates the evolution of seepage area, normalized by catchment area, as a function of $\frac{K}{R}$ for all 60 catchments. Four specific catchments are highlighted with sharper lines for further discussion. As expected, lower $\frac{K}{R}$ values result in fully saturated catchments, while as $\frac{K}{R}$ increases, all catchments progressively desaturate at varying rates. For instance, at a normalized seepage area of 20%, the corresponding $\frac{K}{R}$ values range from 20 to 250.

The desaturation behavior can be clearly differentiated for the 3 clusters of catchments (Figure 3a), confirming that variations in seepage distribution are predominantly driven by topographical effects. The power law fit of seepage distribution (Equation 3a) for each of the 60 catchments results in λ values ranging from 2.05 to 37.03 and n values ranging from -0.44 to -0.31. The fit shows minimal RMSE values between 0.01 and 0.08, indicating that seepage evolution with increasing $\frac{K}{R}$ can be successfully parameterized with only two parameters, λ and n.

Regarding the desaturation threshold, λ , the mountain catchments show lower values than the flat ones. The transitional catchments show intermediate behavior, reaching higher λ values than the mountain catchments but lower than the flat ones. Regarding the desaturation exponent n, within the low-saturation domain ($\leq 20\%$), the mountain catchments exhibit slower desaturation rates, while the flats present faster desaturation rates. The variability in desaturation slopes for the transitional catchments is more pronounced, reflecting a mix of behaviors within this zone, yet it again shows intermediate behavior relative to the other two clusters.

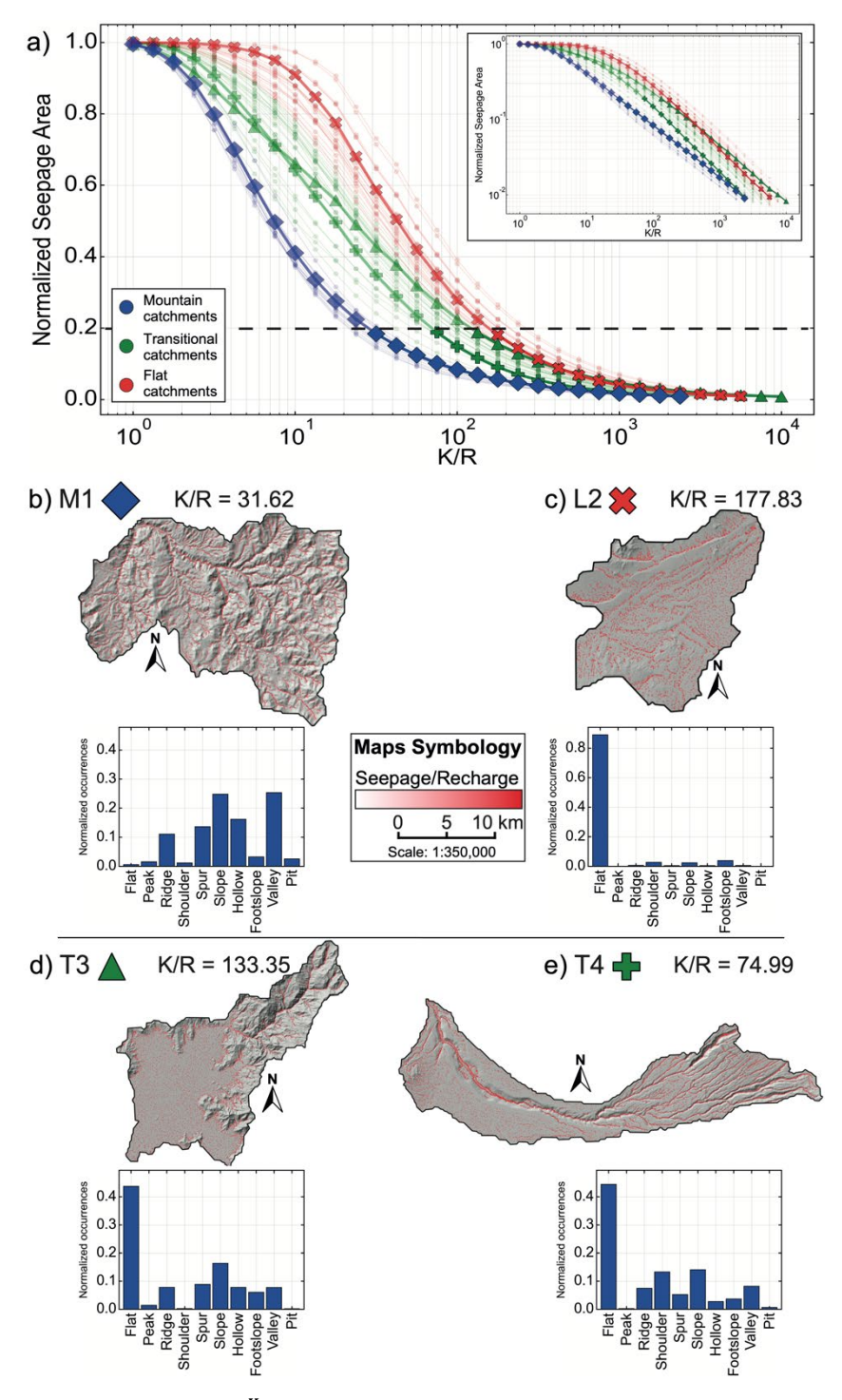


Figure 3: (a) Normalized seepage area against $\frac{K}{R}$ for the 60 catchments (colored lines with markers), including log-log plot on the upper-right corner. Four illustrative catchments are highlighted: mountain type M1 (blue diamond, (b)), flat type F2 (red cross, (c)),

transitional type T3 (green triangle, (d)) and T4 (green cross, (e)). Details include the topographic map overlayed by the seepage extent at an arbitrary value of 20% (red mask) with corresponding $\frac{K}{R}$ value along with the landforms distribution statistics.

3.3. Groundwater seepage extent in four representative catchments

210

215

230

Figure 3 highlights four distinct catchments: M1, representative of the mountain catchments; F2, representing the flat catchments; and T3 and T4, showing the range of responses within the transitional catchments. We present the seepage over recharge distribution overlayed on the topographic map and the landform proportions for each catchment (Figure 3b, c, d, and e).

For M1 (Figure 3b), characterized by low λ and high n values, it exhibits the typical seepage distribution of mountainous regions. At a normalized area of 0.2, seepage primarily congregates in topographic lows, such as river valleys, while ridges and peaks desaturate due to their significant elevation compared to the surrounding terrain. Conversely, F2 (Figure 3c), with high λ and low n values, suggests that the water table remains closer to the surface in flat settings. For T3 and T4, their landform proportions (Figure 3d and e) reveal similar values for most forms, except for a higher proportion of *shoulder* and *footslope* forms in T4. This increased prevalence of *shoulder* landform in T4 is due to a prominent incised river valley in the eastern part of the catchment.

Examining T3's seepage distribution, it initially aligns with the mountain catchments with a low desaturation threshold (λ). Then, in the range of $1 < \frac{\kappa}{R} < 10$, a substantial change in the desaturation function is observed, with the distribution pattern converging toward the ones typical of the flat catchments for high $\frac{\kappa}{R}$ values, ultimately being the last catchment to reach a saturation level of <1%. This behavior can be explained by looking at the spatial distribution of seepage for T3 (Figure 3d). A clear contrast exists between the flat western area and the mountainous settings to the east. At higher elevations, desaturation occurs at lower $\frac{\kappa}{R}$ values dominated by the steep landforms of the mountain settings and resulting in a low desaturation threshold (λ). Subsequently, at a normalized area of 0.2, the catchment desaturation is mostly controlled by the western flat terrains.

Conversely, T4's seepage distribution exhibits an opposite pattern. It initially mirrors the flat cluster with a higher λ value, ultimately resembling the mountain cluster characteristics, reaching saturation levels under 1% for similar $\frac{K}{R}$ values. The seepage spatial distribution for T4 (Figure 3e) shows that flat landforms at higher elevation zones in the western part of the catchment control the initiation of the desaturation before being mostly controlled by the steep incised valley at lower elevations that tends to sustain the seepage extent.

3.4. Linking topographic features and desaturation behavior

We computed the correlation matrix between the principal components (PC1 and PC2) and the desaturation parameters (λ and n) to assess the strength of the topographical control on desaturation behavior. Figure 4a shows a strong anti-correlation

between λ and PC1, with a Spearman coefficient of r = -0.96 (p < 0.0001). Figure 4b displays a strong linear correlation between n and PC1, with r = 0.76 (p < 0.0001). No other significant correlations were identified (the entire correlation matrix is available in Supplementary Material S1).

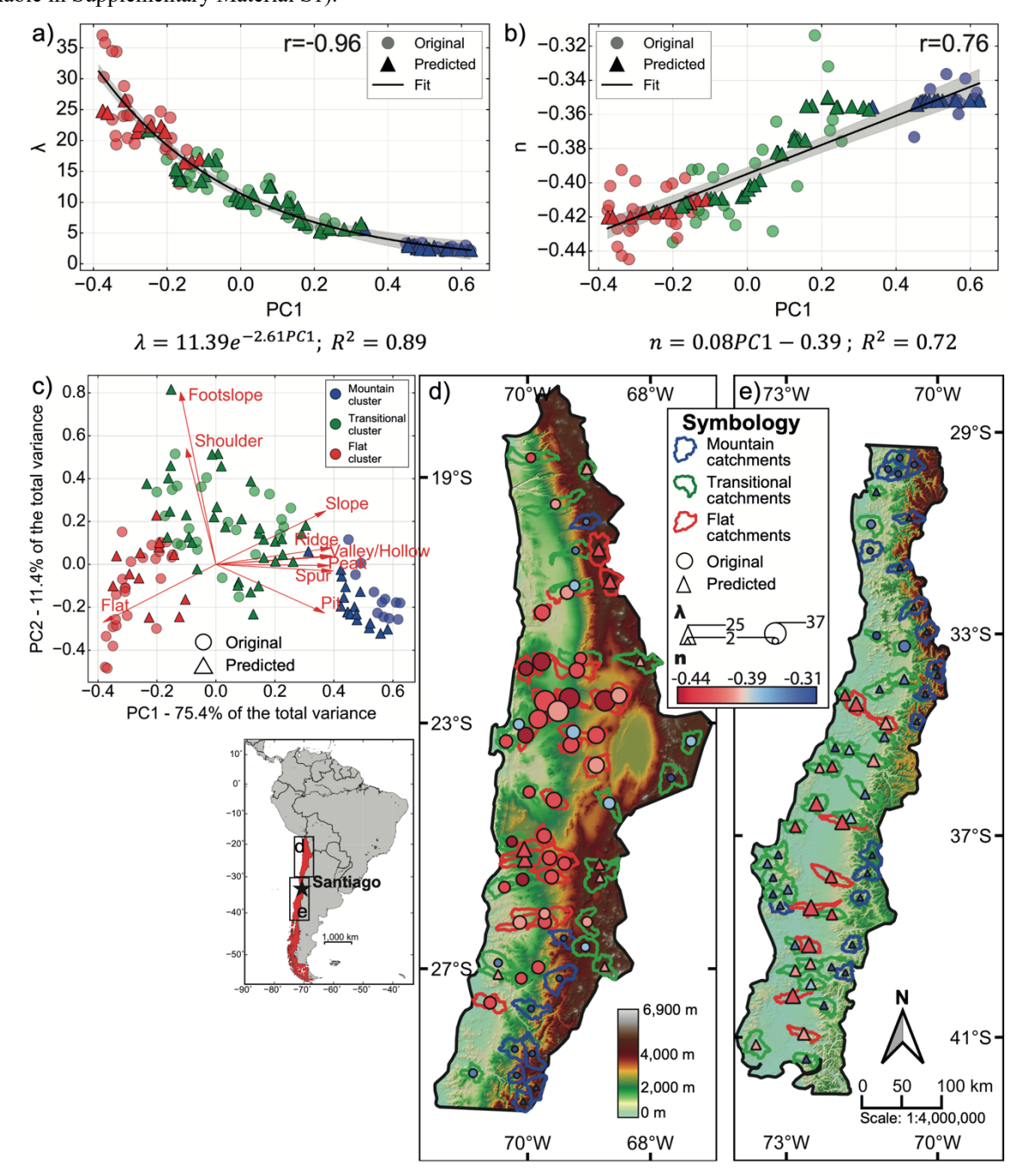


Figure 4: Scatter plots for the original 60-catchment dataset (dots) with Spearman coefficient r, the equation and the coefficient of determination (\mathbb{R}^2) of a global fit (black line with 95% confidence interval) for (a) λ against PC1 and for (b) n against PC1. Random

Forest predictions for both parameters are overlayed on the original data (triangles). (c) PCA plot, for the original (dots) and the prediction (triangles) datasets. The percentage of variance in the original dataset explained by each component is displayed on axis title. (d) and (e) Situation and topographic maps of the study area highlighting the 123 catchments with a colored according to the defined catchment clusters (flat, transitional and mountain). Each catchment is overlayed by a dot (original dataset) or a triangle (prediction dataset) whose size depends on λ and color on n.

The catchment clusters are well distinguishable in Figure 4a and 4b. In Figure 4a, the inverse relationship between λ and PC1 is robustly quantified by fitting an exponential function (R² = 0.89), facilitating a quantitative correlation between λ and PC1, as illustrated in Figure 4a. The mountain cluster is isolated with a low average and variance in λ values. The transitional cluster forms the elbow part of the exponential decay, while the flat cluster is clearly identified with higher λ values. The variations in λ values are higher in the flat and transitional catchments compared to the mountain ones.

Figure 4b reveals a linear relationship between n and PC1. The good linear fit ($R^2 = 0.72$) allows for a straightforward quantification of the relationship between PC1 and the negative scaling exponent n and, consequently, the appraisal of the desaturation rate based on landforms ((2b and 2c)). The catchment clusters are well identified, with the flat cluster showing lower n values than the mountain cluster.

We finally employed a Random Forest regression on the dataset to predict λ and n based on topographic parameters (PC1 and PC2) for 63 catchments located both in the same study area and expanding further South inside Chile (Figure 4d and 4e). We defined PC1, PC2, and clusters for these new catchments using the originally trained PCA and k-means models (Figure 4c). Predictions made for λ (Figure 4a) show good consistency with the original dataset both in terms of identifying clusters behaviors and in trend, following the originally defined exponential relation. Regarding n (Figure 4b), we observe a similar accuracy to represent clusters, while the general linear trend is less obvious. We observe for n, while following an increasing trend, diversified response between the clusters with the transitional catchments exhibiting a greater rate of change in n for an equivalent increment in PC1. Yet the spatial distribution of the predicted catchments observed on Figure 4d and 4e, is a good match with the original data, both in terms of topographic characteristics and desaturation function parameters.

4. Discussion and perspectives

245

250

Groundwater flow and storage regulate the resilience of wetlands to climate variability (Fan et al., 2019). Variations in topography and landforms across catchments lead to differences in wetland sensitivity to changing recharge by shaping distinct groundwater flow structures. In this study, we provide a quantitative assessment of the controls of landforms on the sensitivity of groundwater-dependent wetlands to aquifer desaturation – expressed through variations in the $\frac{K}{R}$ ratio - across a total of 123 catchments in Chile, spanning settings from flat to high mountain topographies. These feedback mechanisms were analyzed using a novel combination of three-dimensional process-based groundwater modeling, geomorphon-based landform classification, multivariate statistical analysis, and Random Forest predictions at the regional scale.

Moreover, the proposed methodology demonstrated strong robustness to outliers and atypical landscape configurations. For instance, the Andes Mountains in northern Chile encompass the "Altiplano" region, which features extensive flat terrains

within an otherwise mountainous setting. The method successfully identified such catchments and classified them as *flat* 275 (Figure 4d between 19 and 23°S), illustrating its ability to reliably capture dominant landform characteristics across diverse geomorphological contexts.

Our results demonstrate that the desaturation functions of catchments can be explained by the typologies in topography derived from landform categorization. Building on previous works that focused on two-dimensional aquifer geometry, as first introduced by Haitjema and Mitchell-Brucker (2005) and further explored by Bresciani et al. (2014), we show that mountainous regions exhibit lower seepage extents, restricted to incised valleys, compared to flat catchments at equivalent $\frac{K}{R}$ ratios. However, we demonstrate that mountainous regions are less sensitive to changes in saturation, exhibiting slower desaturation rates.

280

285

290

295

300

305

To disentangle the respective impacts of different landforms, we compared our results with those obtained from the analytical solution proposed by Bresciani et al. (2014) for a 1D hillslope, where one can easily assess the impacts of slope angle and the concavity/convexity of the hillslope (results in Supplementary Material S3). In agreement with our results, the steepness of the hillslope is the primary influence on seepage extent and its variation through changes in groundwater level. Steep slopes begin to desaturate at lower $\frac{K}{R}$ values than gentler slopes. Additionally, for a given change in groundwater level, the rate of change in seepage extent is inversely correlated with slope angle. This aligns with the differences in the desaturation exponent, n, and the desaturation threshold, λ , obtained for the mountain and flat clusters. Mountain clusters have higher n and λ values, suggesting higher resilience to changes in $\frac{K}{R}$.

Furthermore, the analysis of the simple analytical solution demonstrates that hillslope shape (concave vs. convex) also affects the desaturation function, though to a lesser extent than slope. Concave slopes appear to have a lower λ but a higher n than convex slopes. Similarities between concave and convex hillslopes can be found in the *shoulder* vs. *footslope* in our landform classification. *Shoulder* and *footslope* is differentiated primarily along PC2, explaining a smaller proportion of the variance in the dataset analyzed here. However, no clear correlation between PC2, n, and λ was found, suggesting a minimal impact of *shoulder* and *footslope landforms* compared to the other ones.

While the aim of the present work is to establish a comprehensive exploration of landform controls on seepage dynamics, several simplifications limit its direct application to specific real-catchment systems. Although the models are based on real topographies from the Chilean Andes, the experiment does not intend to capture actual complexity of hydrogeological systems, but rather to explore a wide enough range of natural landform geometries for comparative analysis. First, we assumed homogeneous and isotropic aquifer properties with a fixed aquifer thickness, thereby neglecting geological heterogeneities, anisotropy, and variability in the depth of the active groundwater flow system (Frisbee et al., 2017; McIntosh & Ferguson, 2021), and consequently the seepage distribution, that can be involved in real landscape. While our use of the dimensionless $\frac{K}{R}$ ratio offers a robust approach for analyzing desaturation responses, future research could benefit from exploring additional parameters that account for catchment geometry, relief, or flow system depth. Additionally, the model results presented here

operate under steady-state conditions and exclude the potential impacts of seasonal recharge variability, vegetation feedbacks, or the role of the unsaturated zone near the land surface. Exploring such processes, especially under transient conditions and with heterogeneous parameters, represents a promising perspective for future research.

5. Conclusion

To conclude, our study demonstrates that catchment-scale topographic features, quantified through geomorphon-based landform classification, exert a first-order control on groundwater seepage dynamics under varying recharge conditions. By linking these landforms to a desaturation function, we show that the sensitivity of groundwater seepage extent to climate variability can be predicted from topography alone. This insight enables the development of a robust and scalable framework for assessing hydroclimatic vulnerability, particularly relevant for data-scarce regions. The ability to regionalize desaturation behavior using simple statistical learning tools, such as Random Forests as presented here, opens up new opportunities for applying this approach to ungauged basins in other regions (Hrachowitz et al., 2013). As such, our findings offer not only a methodological advance but also demonstrate potential to assess the vulnerability of groundwater-dependent wetlands and the ecosystem they support to climate change.

Acknowledgments

320

330

We acknowledge funding from the Agencia Nacional de Investigación y Desarrollo (ANID) through grants Fondecyt Regular nº1251067, Anillo nºATE220055, and Anillo nºATE230006.

Open Research

The HydroATLAS global catchments database is freely available at https://www.hydrosheds.org/hydroatlas. The SRTM Digital Elevation model is available on NASA website (https://www.earthdata.nasa.gov/sensors/srtm). Python code to reproduce the analysis, the trained models (PCA, k-means and Random Forest), and the data used to generate results and figures in this manuscript is publicly available at Marti et al (2025). This includes landfoms proportion, PCA, cluster information, λ and n values, and seepage area distribution for each catchment of the original dataset. The predicted dataset is also included (PCA, clusters, λ and n estimations). Catchments ID correspond to the HydroATLAS identification.

335 Competing interests

The contact author has declared that none of the authors has any competing interests.

References

- Abhervé, R., Roques, C., Gauvain, A., Longuevergne, L., Louaisil, S., Aquilina, L., & De Dreuzy, J.-R. (2023). Calibration of groundwater seepage against the spatial distribution of the stream network to assess catchment-scale hydraulic properties. *Hydrology and Earth System Sciences*, 27(17), 3221–3239. https://doi.org/10.5194/hess-27-3221-2023
- Armijo, R., Lacassin, R., Coudurier-Curveur, A., & Carrizo, D. (2015). Coupled tectonic evolution of Andean orogeny and global climate. *Earth-Science Reviews*, 143, 1–35. https://doi.org/10.1016/j.earscirev.2015.01.005
 Bakker, M., Post, V., Langevin, C. D., Hughes, J. D., White, J. T., Starn, J. J., & Fienen, M. N. (2016). Scripting MODFLOW Model Development Using Python and FloPy. *Groundwater*, 54(5), 733–739. https://doi.org/10.1111/gwat.12413
- Barron, O. V., Emelyanova, I., Van Niel, T. G., Pollock, D., & Hodgson, G. (2014). Mapping groundwater-dependent ecosystems using remote sensing measures of vegetation and moisture dynamics: GDES MAPPING USING REMOTE MEASURES OF VEGETATION/MOISTURE DYNAMICS. *Hydrological Processes*, 28(2), 372–385. https://doi.org/10.1002/hyp.9609
- Berghuijs, W. R., Collenteur, R. A., Jasechko, S., Jaramillo, F., Luijendijk, E., Moeck, C., Van Der Velde, Y., & Allen, S. T. (2024). Groundwater recharge is sensitive to changing long-term aridity. *Nature Climate Change*, *14*(4), 357–363. https://doi.org/10.1038/s41558-024-01953-z
 - Bresciani, E., Davy, P., & de Dreuzy, J.-R. (2014). Is the Dupuit assumption suitable for predicting the groundwater seepage area in hillslopes? *Water Resources Research*, 50(3), 2394–2406. https://doi.org/10.1002/2013WR014284
 - Bresciani, E., Goderniaux, P., & Batelaan, O. (2016). Hydrogeological controls of water table-land surface interactions: Water
- Table-Land Surface Interactions. *Geophysical Research Letters*, 43(18), 9653–9661. https://doi.org/10.1002/2016GL070618 Carlier, C., Wirth, S. B., Cochand, F., Hunkeler, D., & Brunner, P. (2019). Exploring Geological and Topographical Controls on Low Flows with Hydrogeological Models. *Groundwater*, 57(1), 48–62. https://doi.org/10.1111/gwat.12845 Charrier, R., Pinto, L., & Rodríguez, M. P. (2007). Tectonostratigraphic evolution of the Andean Orogen in Chile. In T. Moreno
- & W. Gibbons (Eds.), *The Geology of Chile* (First, pp. 21–114). The Geological Society of London. https://doi.org/10.1144/GOCH.3
- Condon, L. E., Markovich, K. H., Kelleher, C. A., McDonnell, J. J., Ferguson, G., & McIntosh, J. C. (2020). Where Is the Bottom of a Watershed? *Water Resources Research*, 56(3), e2019WR026010. https://doi.org/10.1029/2019WR026010 Condon, L. E., & Maxwell, R. M. (2015). Evaluating the relationship between topography and groundwater using outputs from a continental-scale integrated hydrology model. *Water Resources Research*, 51(8), 6602–6621.
- https://doi.org/10.1002/2014WR016774
 Cuthbert, M. O., Gleeson, T., Moosdorf, N., Befus, K. M., Schneider, A., Hartmann, J., & Lehner, B. (2019). Global patterns and dynamics of climate–groundwater interactions. *Nature Climate Change*, 9(2), 137–141. https://doi.org/10.1038/s41558-018-0386-4
- Doody, T. M., Barron, O. V., Dowsley, K., Emelyanova, I., Fawcett, J., Overton, I. C., Pritchard, J. L., Van Dijk, A. I. J. M., & Warren, G. (2017). Continental mapping of groundwater dependent ecosystems: A methodological framework to integrate diverse data and expert opinion. *Journal of Hydrology: Regional Studies*, 10, 61–81. https://doi.org/10.1016/j.ejrh.2017.01.003 Eamus, D., & Froend, R. (2006). Groundwater-dependent ecosystems: The where, what and why of GDEs. *Australian Journal of Botany*, 54(2), 91. https://doi.org/10.1071/BT06029 Fan, Y. (2019). Are catchments leaky? *WIREs Water*, 6(6). https://doi.org/10.1002/wat2.1386
- 575 Fan, Y., Clark, M., Lawrence, D. M., Swenson, S., Band, L. E., Brantley, S. L., Brooks, P. D., Dietrich, W. E., Flores, A., Grant, G., Kirchner, J. W., Mackay, D. S., McDonnell, J. J., Milly, P. C. D., Sullivan, P. L., Tague, C., Ajami, H., Chaney, N., Hartmann, A., ... Yamazaki, D. (2019). Hillslope Hydrology in Global Change Research and Earth System Modeling. *Water Resources Research*, 55(2), 1737–1772. https://doi.org/10.1029/2018WR023903
- Frisbee, M. D., Tolley, D. G., & Wilson, J. L. (2017). Field estimates of groundwater circulation depths in two mountainous watersheds in the western U.S. and the effect of deep circulation on solute concentrations in streamflow. *Water Resources Research*, 53(4), 2693–2715. https://doi.org/10.1002/2016WR019553

 Gauvain, A., Leray, S., Marçais, J., Roques, C., Vautier, C., Gresselin, F., Aquilina, L., & Dreuzy, J. (2021). Geomorphological
 - Gauvain, A., Leray, S., Marçais, J., Roques, C., Vautier, C., Gresselin, F., Aquilina, L., & Dreuzy, J. (2021). Geomorphological Controls on Groundwater Transit Times: A Synthetic Analysis at the Hillslope Scale. *Water Resources Research*, *57*(7). https://doi.org/10.1029/2020WR029463
- 385 Gleeson, T., & Manning, A. H. (2008). Regional groundwater flow in mountainous terrain: Three-dimensional simulations of

- topographic and hydrogeologic controls. *Water Resources Research*, 44(10). https://doi.org/10.1029/2008WR006848 Haitjema, H. M., & Mitchell-Bruker, S. (2005). Are Water Tables a Subdued Replica of the Topography? *Groundwater*, 43(6), 781–786. https://doi.org/10.1111/j.1745-6584.2005.00090.x
- Harbaugh, A. W. (2005). MODFLOW-2005: The U.S. Geological Survey modular ground-water model—The ground-water flow process (Report 6-A16; Techniques and Methods). USGS Publications Warehouse. https://doi.org/10.3133/tm6A16
 Hartley, A. J., & Evenstar, L. (2010). Cenozoic stratigraphic development in the north Chilean forearc: Implications for basin development and uplift history of the Central Andean margin. Tectonophysics, 495(1–2), 67–77. https://doi.org/10.1016/j.tecto.2009.05.013
- Hrachowitz, M., Savenije, H. H. G., Blöschl, G., McDonnell, J. J., Sivapalan, M., Pomeroy, J. W., Arheimer, B., Blume, T., Clark, M. P., Ehret, U., Fenicia, F., Freer, J. E., Gelfan, A., Gupta, H. V., Hughes, D. A., Hut, R. W., Montanari, A., Pande, S., Tetzlaff, D., ... Cudennec, C. (2013). A decade of Predictions in Ungauged Basins (PUB)—A review. *Hydrological Sciences Journal*, *58*(6), 1198–1255. https://doi.org/10.1080/02626667.2013.803183
 - Jamieson, G. R., & Freeze, R. A. (1982). Determining Hydraulic Conductivity Distributions in a Mountainous Area Using Mathematical Modeling. *Ground Water*, 20(2), 168–177. https://doi.org/10.1111/j.1745-6584.1982.tb02745.x
- Jasiewicz, J., & Stepinski, T. F. (2013). Geomorphons—A pattern recognition approach to classification and mapping of landforms. *Geomorphology*, 182, 147–156. https://doi.org/10.1016/j.geomorph.2012.11.005
 Jordan, T. E., Isacks, B. L., Allmendinger, R. W., Brewer, J. A., Ramos, V. A., & Ando, C. J. (1983). Andean tectonics related to geometry of subducted Nazca plate. *Geological Society of America Bulletin*, 94(3), 341. https://doi.org/10.1130/0016-7606(1983)94<341:ATRTGO>2.0.CO:2
- Jordan, T. E., Kirk-Lawlor, N. E., Blanco, N. P., Rech, J. A., & Cosentino, N. J. (2014). Landscape modification in response to repeated onset of hyperarid paleoclimate states since 14 Ma, Atacama Desert, Chile. *Geological Society of America Bulletin*, 126(7–8), 1016–1046. https://doi.org/10.1130/B30978.1
 - Kløve, B., Ala-aho, P., Bertrand, G., Boukalova, Z., Ertürk, A., Goldscheider, N., Ilmonen, J., Karakaya, N., Kupfersberger, H., Kværner, J., Lundberg, A., Mileusnić, M., Moszczynska, A., Muotka, T., Preda, E., Rossi, P., Siergieiev, D., Šimek, J.,
- Wachniew, P., ... Widerlund, A. (2011). Groundwater dependent ecosystems. Part I: Hydroecological status and trends. *Environmental Science & Policy*, 14(7), 770–781. https://doi.org/10.1016/j.envsci.2011.04.002
 Kløve, B., Ala-Aho, P., Bertrand, G., Gurdak, J. J., Kupfersberger, H., Kværner, J., Muotka, T., Mykrä, H., Preda, E., Rossi, P., Uvo, C. B., Velasco, E., & Pulido-Velazquez, M. (2014). Climate change impacts on groundwater and dependent ecosystems. *Journal of Hydrology*, 518, 250–266. https://doi.org/10.1016/j.jhydrol.2013.06.037
- Konapala, G., Mishra, A. K., Wada, Y., & Mann, M. E. (2020). Climate change will affect global water availability through compounding changes in seasonal precipitation and evaporation. *Nature Communications*, 11(1), 3044. https://doi.org/10.1038/s41467-020-16757-w
 - Lehner, B., & Grill, G. (2013). Global river hydrography and network routing: Baseline data and new approaches to study the world's large river systems. *Hydrological Processes*, 27(15), 2171–2186. https://doi.org/10.1002/hyp.9740
- Lindsay, J. B. (2016). Whitebox GAT: A case study in geomorphometric analysis. Computers & Geosciences, 95, 75–84. https://doi.org/10.1016/j.cageo.2016.07.003
 Marçais, J., De Dreuzy, J.-R., & Erhel, J. (2017). Dynamic coupling of subsurface and seepage flows solved within a regularized partition formulation. Advances in Water Resources, 109, 94–105. https://doi.org/10.1016/j.advwatres.2017.09.008
- Marti, E., Leray, S., & Roques, C. (2025). Dataset used in "Catchment landforms predict groundwater-dependent wetland sensitivity to recharge changes", manuscript submitted to HESS. [Dataset]. Zenodo. https://doi.org/10.5281/ZENODO.10144981
 McIntosh, J. C., & Ferguson, G. (2021). Deep Meteoric Water Circulation in Earth's Crust. Geophysical Research Letters, 48(5), e2020GL090461. https://doi.org/10.1029/2020GL090461
- 430 Nester, P., & Jordan, T. (2011). The Pampa del Tamarugal Forearc Basin in Northern Chile: The Interaction of Tectonics and Climate. In C. Busby & A. Azor (Eds.), *Tectonics of Sedimentary Basins* (1st ed., pp. 369–381). Wiley. https://doi.org/10.1002/9781444347166.ch18
 Niswonger, R. G., Panday, S., & Ibaraki, M. (2011). *MODFLOW-NWT, a Newton formulation for MODFLOW-2005* (Report 6-A37; Techniques and Methods). USGS Publications Warehouse. https://doi.org/10.3133/tm6A37
- 435 Pedregosa, F., Varoquaux, G., Gramfort, A., Michel, V., Thirion, B., Grisel, O., Blondel, M., Prettenhofer, P., Weiss, R.,

- Dubourg, V., Vanderplas, J., Passos, A., Cournapeau, D., Brucher, M., Perrot, M., & Duchesnay, É. (2011). Scikit-learn: Machine Learning in Python. *Journal of Machine Learning Research*, 12(85), 2825–2830.
- Rath, P., Bresciani, E., Zhu, J., & Befus, K. M. (2023). Numerical analysis of seepage faces and subaerial groundwater discharge near waterbodies and on uplands. *Environmental Modelling & Software*, 169, 105828.
- https://doi.org/10.1016/j.envsoft.2023.105828
 Rohde, M. M., Albano, C. M., Huggins, X., Klausmeyer, K. R., Morton, C., Sharman, A., Zaveri, E., Saito, L., Freed, Z., Howard, J. K., Job, N., Richter, H., Toderich, K., Rodella, A.-S., Gleeson, T., Huntington, J., Chandanpurkar, H. A., Purdy,
 - A. J., Famiglietti, J. S., ... Stella, J. C. (2024). Groundwater-dependent ecosystem map exposes global dryland protection needs. *Nature*, 632(8023), 101–107. https://doi.org/10.1038/s41586-024-07702-8
- 445 Scanlon, B. R., Fakhreddine, S., Rateb, A., De Graaf, I., Famiglietti, J., Gleeson, T., Grafton, R. Q., Jobbagy, E., Kebede, S., Kolusu, S. R., Konikow, L. F., Long, D., Mekonnen, M., Schmied, H. M., Mukherjee, A., MacDonald, A., Reedy, R. C., Shamsudduha, M., Simmons, C. T., ... Zheng, C. (2023). Global water resources and the role of groundwater in a resilient water future. *Nature Reviews Earth & Environment*, 4(2), 87–101. https://doi.org/10.1038/s43017-022-00378-6
 - Singha, K., & Navarre-Sitchler, A. (2022). The Importance of Groundwater in Critical Zone Science. *Groundwater*, 60(1),
- 450 27–34. https://doi.org/10.1111/gwat.13143 Sophocleous, M. (2002). Interactions between groundwater and surface water: The state of the science. *Hydrogeology Journal*, 10(1), 52–67. https://doi.org/10.1007/s10040-001-0170-8
 - Taylor, R. G., Scanlon, B., Döll, P., Rodell, M., van Beek, R., Wada, Y., Longuevergne, L., Leblanc, M., Famiglietti, J. S., Edmunds, M., Konikow, L., Green, T. R., Chen, J., Taniguchi, M., Bierkens, M. F. P., MacDonald, A., Fan, Y., Maxwell, R.
- 455 M., Yechieli, Y., ... Treidel, H. (2013). Ground water and climate change. *Nature Climate Change*, 3(4), 322–329. https://doi.org/10.1038/nclimate1744
 - Tetzlaff, D., Laudon, H., Luo, S., & Soulsby, C. (2024). Ecohydrological resilience and the landscape water storage continuum in droughts. *Nature Water*, 2(10), 915–918. https://doi.org/10.1038/s44221-024-00300-y
 - Tóth, J. (1963). A theoretical analysis of groundwater flow in small drainage basins. *Journal of Geophysical Research*, 68(16), 4795–4812. https://doi.org/10.1029/JZ068i016p04795
- 460 4795–4812. https://doi.org/10.1029/JZ068i016p04795
 Welch, L. A., Allen, D. M., & Van Meerveld, H. J. (2012). Topographic Controls on Deep Groundwater Contributions to Mountain Headwater Streams and Sensitivity to Available Recharge. Canadian Water Resources Journal / Revue Canadienne Des Ressources Hydriques, 37(4), 349–371. https://doi.org/10.4296/cwrj2011-907
 - Yáñez, G., Munoz, M., Flores-Aqueveque, V., & Bosch, A. (2015). Gravity derived depth to basement in Santiago Basin,
- 465 Chile: Implications for its geological evolution, hydrogeology, low enthalpy geothermal, soil characterization and geo-hazards. *Andean Geology*, 42(2), 147–172. https://doi.org/10.5027/andgeoV42n2-a01
 - Zhang, X., Jiao, J. J., & Guo, W. (2022). How Does Topography Control Topography-Driven Groundwater Flow? *Geophysical Research Letters*, 49(20), e2022GL101005. https://doi.org/10.1029/2022GL101005